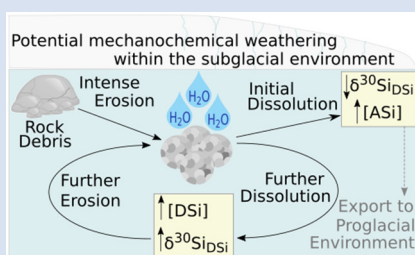# Physical weathering by glaciers enhances silicon mobilisation and isotopic fractionation

J.E. Hatton[1,2*], K.R. Hendry[2], J.R. Hawkings[3,4], J.L. Wadham[5,6], L.G. Benning[4,7], R. Blukis[4], V. Roddatis[4], H.C. Ng[2], T. Wang[2]

OPEN ACCESS

Abstract

Glacial meltwaters export substantial quantities of dissolved and dissolvable amorphous silicon (DSi and ASi), providing an essential nutrient for downstream diatoms. Evidence suggests that glacially exported DSi is isotopically light compared to DSi in non-glaciated rivers. However, the isotopic fractionation mechanisms are not well constrained, indicating an important gap in our understanding of processes in the global Si cycle. We use rock crushing experiments to mimic subglacial physical erosion, to provide insight into subglacial isotope fractionation. Isotopically light DSi ($\delta^{30}Si_{DSi}$) released following initial dissolution of freshly ground mineral surfaces (down to -2.12 ± 0.02 ‰) suggests mechanochemical reactions induce isotopic fractionation, explaining the low $\delta^{30}Si_{DSi}$ composition of subglacial runoff. ASi with a consistent isotopic composition is present in all mechanically weathered samples, but concentrations are elevated in samples that have undergone more intense physical grinding. These experiments illustrate the critical role of physical processes in driving isotopic fractionation and biogeochemical weathering in subglacial environments. Understanding perturbations in high latitude Si cycling under climatic change will likely depend on the response of mechanochemical weathering to increased glacial melt.

Introduction

Glaciers and ice sheets are dynamic sources of nutrients and reactive particulate material to downstream ecosystems (*e.g.,* Wadham *et al.,* 2010; Hawkings *et al.,* 2015; Sharp and Tranter, 2017). There is evidence that silicate mineral weathering is enhanced beneath large ice sheets (Wadham *et al.,* 2010; Michaud *et al.,* 2016), which may contribute significant fluxes of dissolved silicon and dissolvable amorphous silica (DSi and ASi respectively) downstream, stimulating productivity of siliceous organisms (Hendry *et al.,* 2019).

The stable silicon isotopic composition (denoted by $\delta^{30}Si$) of glacial meltwaters can aid mechanistic understanding of subglacial weathering processes (Opfergelt *et al.,* 2013; Hawkings *et al.,* 2018; Hatton *et al.,* 2019a). Previous work has hypothesised that physical weathering in the subglacial environment results in isotopically light DSi in glacial meltwaters when compared to non-glacial riverine waters (Hatton *et al.,* 2019b). This is likely due to the creation of highly reactive mineral surfaces combined with chemical precipitation-dissolution reactions, which result in the formation and preferential dissolution of isotopically depleted amorphous weathering crusts (Opfergelt *et al.,* 2013;

Hatton *et al.,* 2019b). The high levels of physical erosion and sediment comminution in subglacial environments, combined with chemical weathering act to enhance the export of DSi from subglacial environments. However, a better understanding of subglacial silicate dissolution and associated Si isotopic fractionation is required to constrain the impacts of changing glacial environments on wider associated elemental cycles (*e.g.,* nutrient liberation from silicate minerals and long term carbon drawdown from silicate weathering) and enable the inclusion of glacially exported Si in global biogeochemical models.

A large proportion of the glacial Si flux is likely exported as ASi. Field observations from Leverett Glacier, Greenland reveal up to 95 % of Si exported is ASi, which is soluble in downstream marine environments (Hawkings *et al.,* 2017). The potential ASi formation mechanisms to explain elevated glacial ASi concentrations include dissolution-reprecipitation weathering where ASi forms *via* supersaturation at the grain boundary (Hellmann *et al.,* 2012), and chemically leached particle surface layers resulting in an amorphous crust of less soluble ions such as Si (Casey *et al.,* 1993). Additionally, silicate dissolution and ASi formation have been linked to physical processes, with ASi hypothesised to form as a disturbed surface layer (Blackburn *et al.,* 2019; Hatton *et al.,*

1. Department of Ecology, Faculty of Science, Charles University, Prague, Czech Republic
2. School of Earth Sciences, University of Bristol, Wills Memorial Building, Queens Road, Bristol, UK
3. Department of Earth and Environmental Science, University of Pennsylvania, Hayden Hall, 240 South 33rd Street, Philadelphia, PA 19104, USA
4. German Research Centre for Geosciences GFZ, 14473, Potsdam, Germany
5. School of Geographical Sciences, University of Bristol, Bristol, UK
6. Centre for Arctic Gas Hydrate, Environment and Climate (CAGE), Department of Geosciences, UiT The Arctic University of Norway, N-9037 Tromsø, Norway
7. Department of Earth Sciences, Free University of Berlin, 12249, Berlin, Germany
* Corresponding author (email: jade.hatton@natur.cuni.cz)

2019b). This combination of physical erosion and chemical weathering (*i.e.* mechanochemical) could be key to understanding subglacial processes, considering high erosion rates and large surface areas of sediments in subglacial environments.

We tested the hypotheses that high physical erosion rates in subglacial environments result in (i) isotopically light DSi *via* the production of highly reactive fine grained glacial flour (Opfergelt *et al.*, 2013; Hatton *et al.*, 2019b), and (ii) the formation of ASi. Dissolution experiments (Fig. 1) mimicked mechanochemical processes in the subglacial system to ascertain the role of physical weathering on Si concentrations and δ^{30}Si

composition (see Supplementary Information for full methodology). Pre-weathered unsorted glacial till (dominantly plagioclase and quartz; Fig. S-1) from Leverett Glacier proglacial plain (LG; Fig. S-2) was mechanically milled for either 2 (T2) or 30 (T30) minutes in an agate mill (note that ASi concentrations produced when milling in agate or steel mills were within analytical error, showing no significant contamination source from the agate mill, see Supplementary Information) and reacted for up to 720 hours with ultra-pure water (18.2 MΩ cm, Millipore®). The milled and reacted powders were then re-dried, re-crushed and reacted again to mimic ongoing physical erosion within a subglacial
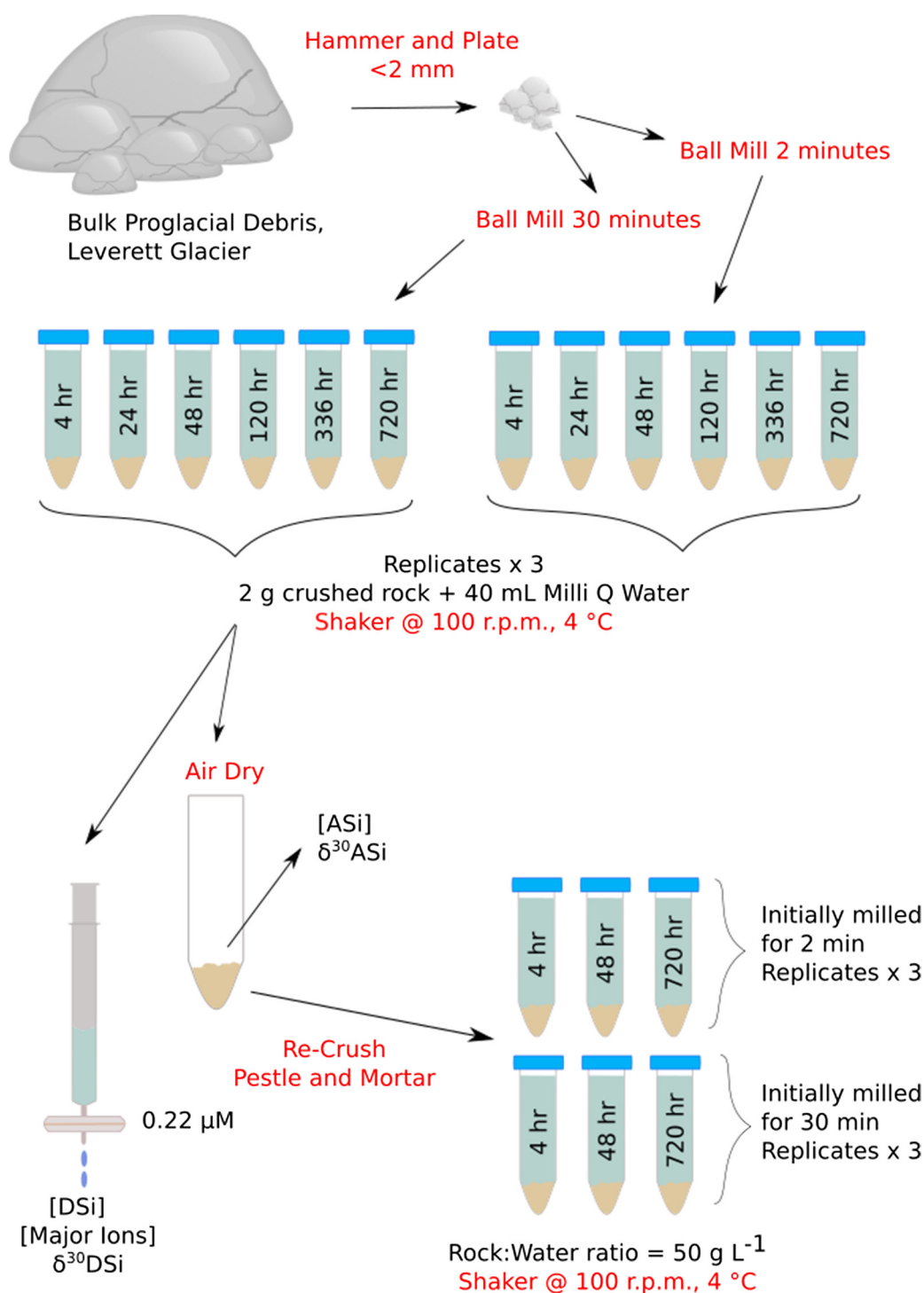

Figure 1 Illustration of the experimental set up.

environment (Fig. 1). We chose to use field collected samples for these experiments to better mimic real world conditions and compare to existing field data.

Results and Discussion

Dissolution of freshly exposed mineral surfaces drives isotopically light DSi. Our experiments highlight the likely importance of physical erosion processes in subglacial environments. Rapid dissolution of Si after initial milling and after re-crushing led to $\delta^{30}Si_{DSi}$ values (down to −2.12 ‰) more depleted than values recorded in subglacial meltwater sourced DSi (+1.01 to −0.58 ‰; Hatton *et al.,* 2019b). The lowest $\delta^{30}Si_{DSi}$ composition for T2 and T30 was measured after 4 hours, with $\delta^{30}Si_{DSi}$ increasing over time (Fig. 2, Table S-1). The preferential release of lighter Si isotopes during dissolution relates to the distribution of ^{28}Si and ^{29}Si on surface layers. Our experiments agree with previous experiments that show physical grinding leads to the preferential release of ^{28}Si during initial dissolution of fresh surface layers, which suggests a higher abundance of ^{28}Si on the surface of freshly ground minerals in the destabilised outer layers of the crystal structure (Ziegler *et al.,* 2005). It's likely that the high

surface areas created by physical grinding led to rapid initial dissolution of Si, with the largest isotopic fractionation. As the experiment progressed, the $\delta^{30}Si_{DSi}$ composition increased toward $\delta^{30}Si_{Bulk}$ values (Fig. 2) as proportionally more ^{29}Si was liberated from internal crystalline structures.

After the reacted material was re-crushed, the $\delta^{30}Si_{DSi}$ composition decreased again (down to −1.29 ‰; Fig. 2, Table S-2). The decrease in $\delta^{30}Si_{DSi}$ composition after re-crushing, suggests that the regeneration of reactive mineral surface layers by physical action promotes further dissolution of isotopically light Si. This process presents a viable mechanism to explain isotopically light DSi in glacial meltwaters, due to the continuous comminution of bedrock in the subglacial system.

Our findings of initial dissolution resulting in low $\delta^{30}Si_{DSi}$ composition are consistent with results of leaching experiments on basaltic lavas (Ziegler *et al.,* 2005) and diatom opal (Demarest *et al.,* 2009), suggesting this process is independent of sediment lithology. While our experiments do not isolate the exact mechanism driving the apparent fractionation during initial dissolution, they do suggest that continuous comminution of subglacial sediments results in exposure of fresh, large surface areas. This reactive surface layer promotes the dissolution of Si and
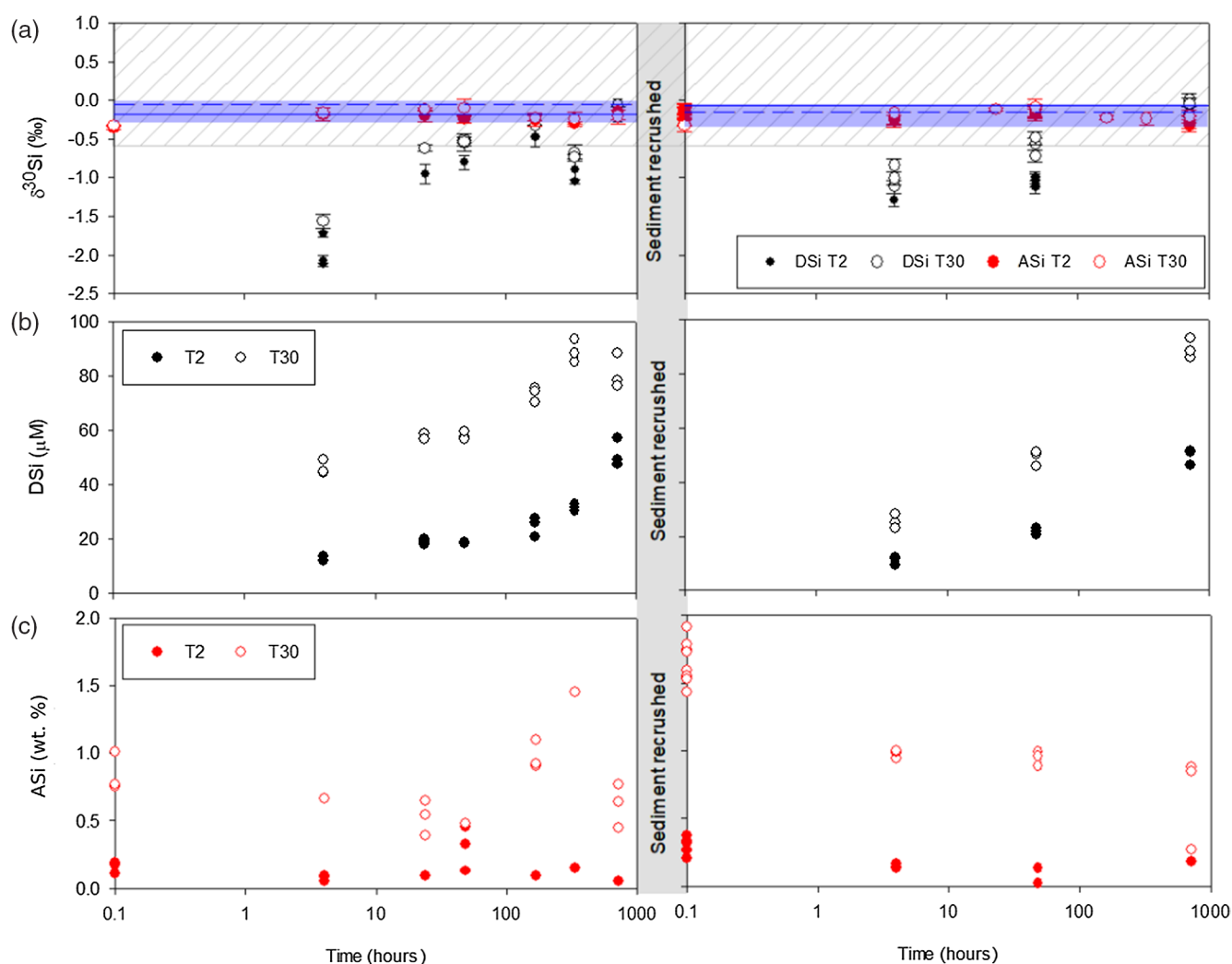

Figure 2   Geochemical results of primary and crushing experiments over time. DSi = black, ASi = red, closed = T2, open = T30. **(a)** $\delta^{30}Si_{DSi}$ and $\delta^{30}Si_{ASi}$ composition, error bars represent average external error (0.08 ‰, 2 s.d.). Blue horizontal lines mark $\delta^{30}Si$ composition of bulk rock (T2 = solid, T30 = dashed), with 2 s.d. external error shaded blue. **(b)** DSi concentrations. **(c)** ASi concentrations. Initial and secondary milled data separated by vertical grey area. Glacial river $\delta^{30}Si_{DSi}$ range from −0.58 to +1.01 ‰ (grey hashed region) and glacial $\delta^{30}Si_{ASi}$ ranges from −0.86 to −0.05 ‰ (Hatton *et al.,* 2019b).

drives the light $\delta^{30}Si_{DSi}$ composition in glacial meltwaters (Opfergelt *et al.*, 2013; Hatton *et al.*, 2019b).

The degree of isotopic fractionation does not appear to scale with DSi concentration and the available surface area. T2 experiments had lighter $\delta^{30}Si_{DSi}$ composition than T30 for all timepoints (Fig. 2), despite lower DSi concentrations (Fig. 2) and lower specific surface area deduced from mean grain size of material (Fig. S-3; Telling *et al.*, 2015). There are potential explanations for this, considering i) isotopic heterogeneity within the starting material, ii) natural pre-weathering of rock material, and/or iii) ASi formation and dissolution. The rocks used in this experiment from the proglacial plain, are naturally heterogeneous, and were pre-weathered within the sub- and pro-glacial environment. We see evidence of amorphous SiO_2 nanoparticles in all samples *via* HR-TEM imaging (see Fig. 4), highlighting a degree of environmental pre-weathering prior to sample collection. This pre-weathering of material could have resulted in surface layers with a lower $\delta^{30}Si$ composition compared to the bulk rock material due to the fractionation induced by weathering processes (Frings *et al.*, 2016). When the rocks were milled for a short time (T2), the fresh mineral surfaces were comparatively enriched with Si from these pre-weathered surfaces (*e.g.*, isotopically light amorphous nanoparticles). Whereas, longer milling in T30 exposed more of the non-weathered crystalline structure from where proportionally more DSi was derived. This could explain why T30 DSi was marginally closer to the bulk rock value (-0.13 ± 0.16 ‰). Alternatively, the higher ASi concentrations in T30 experiments may have impacted the overall $\delta^{30}Si_{DSi}$ composition. Previous experiments have shown large isotopic fractionations (up to -7.5 ‰) associated with quartz cement dissolution and precipitation (Basile-Doelsch *et al.*, 2005). If there was proportionally greater ASi dissolution in T30 experiments, when compared to T2 experiments, then this could have resulted in a smaller overall fractionation in T30 and a less depleted $\delta^{30}Si_{DSi}$ composition.

Our experiments do not allow for a detailed analysis of the difference in $\delta^{30}Si_{DSi}$ composition between T2 and T30 resulting from dissolution, particularly with the potential impacts of the environmental pre-weathering. However, the overall differences are small compared to the large fractionation observed after initial dissolution. Therefore, we hypothesise that continuous subglacial physical erosion of bedrock could lead to isotopically low $\delta^{30}Si_{DSi}$ after wetting sediments with dilute waters. This process would likely explain the observed low meltwater $\delta^{30}Si_{DSi}$ composition (Hatton *et al.*, 2019b).

Mechanochemical reactions may promote ASi formation in subglacial systems. A more robust understanding of the formation process of subglacial ASi is important considering the large flux term of glacial ASi to downstream environments (Hawkings *et al.*, 2017). We use these experiments to deduce the potential role of physical erosion in ASi formation. ASi concentrations were consistently higher in T30 compared to T2 (Fig. 3, Tables S-1, S-2) after both the initial milling (T30 ~ 0.8 % d.w., T2 ~ 0.2 % d.w.) and then re-crushing (T30 ~ 1.2 % d.w., T2 ~ 0.3 % d.w.), indicating that more intense physical erosion and generation of larger particle surface areas resulted in higher observed ASi concentrations. The increase in ASi from the end of the initial dissolution to when the material was re-crushed also indicates that the secondary crushing regenerates fresh amorphous mineral surfaces. It is likely that the milling process results in greater ASi formation, which is more soluble as a result of a greater surface area from longer milling times. Elevated ASi concentrations from crushing are consistent with field observations of ASi-rich precipitates produced by subglacial physical and chemical weathering processes during the last glaciation (Blackburn *et al.*, 2019), and ASi formation by
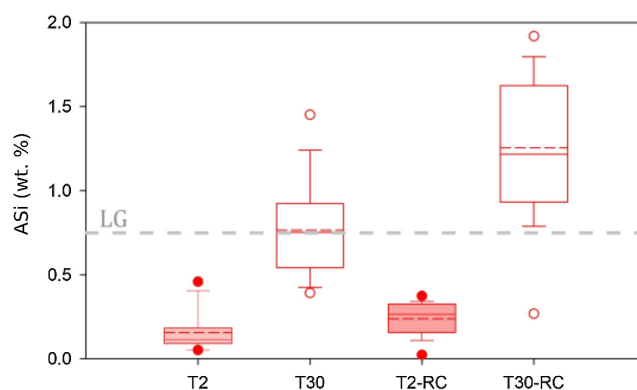

Figure 3 ASi concentrations, grouped as T2, T30 (initial milling and dissolution), and T2-RC, T30-RC (secondary crushing and dissolution), with median (solid) and mean (dashed) shown. Grey dashed line represents discharge weighted mean ASi concentration from proglacial river of Leverett Glacier (LG) in 2015 (Hatton *et al.*, 2019a).

comminution and associated breakdown of crystalline structures (Yund *et al.*, 1990).

A confounding factor is that HR-TEM photomicrographs indicate the presence of amorphous SiO_2 nanoparticle aggregates in all samples (Fig. 4). There was also no statistical difference in overall crystallinity between starting material and milled material when completing pair distribution function (PDF) analysis of the X-ray scattering, though observable peak differences were present (Fig. S-4). These small concentrations of chemically sourced ASi observable under HR-TEM, likely result from environmental pre-weathering. Despite this, the low ASi concentrations of unmilled control experiments (avg. 0.11 % d.w.; Table S-6) combined with the elevated ASi concentrations for all T30 experiments (avg. 1.03 % d.w.), provide strong evidence for the importance of intense physical erosion in amorphisation and the mobilisation of pre-existing reactive Si, mimicking the subglacial environment.

The $\delta^{30}Si_{ASi}$ composition (Fig. 2) was not significantly different over the incubation timescale (ANOVA, p value 0.06), between T2 and T30 (ANOVA, p value 0.83), and after re-crushing (ANOVA, p value 0.87), with an overall average $\delta^{30}Si_{ASi}$ of -0.22 ± 0.15 ‰ (2 s.d.). It is likely that this relatively consistent $\delta^{30}Si_{ASi}$ composition is linked to the large ASi reservoir compared to DSi. Our experimental values are similar in composition to field measurements over a summer melt season at LG (-0.32 to -0.11 ‰; Hatton *et al.*, 2019a), demonstrating the likely similarities between the subglacial processes forming ASi in the field and in our experiments.

Implications for Subglacial Silicon Cycling

Our findings highlight the importance of mechanochemical processes beneath glaciers for silicon cycling despite near freezing water temperatures. Our study improves understanding of the mechanistic drivers of subglacial Si cycling, which will help inform wider biogeochemical models. Our experiments highlight the potential of glacial physical weathering in creating high concentrations of labile ASi and a distinct isotopic signature for DSi. Physical erosion appears essential in creating fresh reactive mineral surfaces that lead to the dissolution of isotopically light DSi in subglacial environments. It is therefore likely that actively eroding glaciers with high suspended sediment concentrations and an active subglacial hydrological system will export
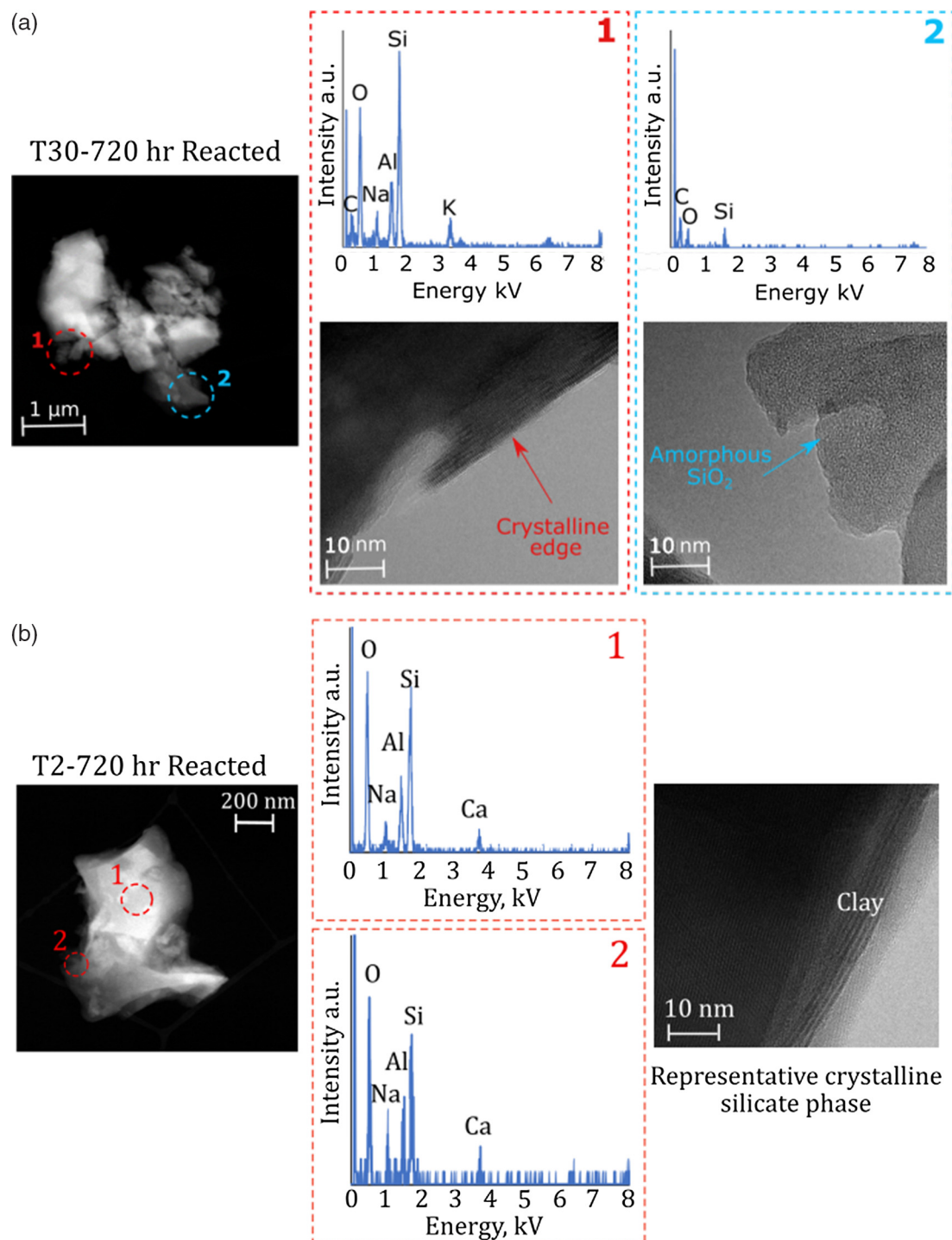
Figure 4 High-resolution transmission electron microscopy (HR-TEM) photomicrographs and energy-dispersive X-ray spectra (EDS) of particles from T30-720 hr and T2-720 hr. **(a1)** Representative crystalline edge and EDS spectra, likely plagioclase. **(a2)** Representative amorphous area, containing Si and O, indicative of ASi. **(b)** Crystalline silicate phases representative of T2-720 hr.

meltwaters with isotopically light DSi compared to non-glacial rivers. The variation in $\delta^{30}Si_{DSi}$ composition and ASi concentrations between glacierised catchments could be explained by differences in erosional processes, such as heterogeneity within and between glacial ice flow rates, subglacial hydrological conditions, starting bedrock composition, and resulting mobilised sediment surface areas. Further work considering mechanistic processes using pristine starting minerals could be beneficial. Such work, combined with our findings would be key to informing a developed conceptual model of glacial biogeochemical weathering processes to consider the sensitivity of glacier and ice sheet melt to climatic warming, and the potential role of these systems in global elemental cycling.

Author Contributions

JEH and KRH conceived the study. JEH, RB, VR, LGB, HCN and TW completed laboratory analysis. All authors were involved in writing the manuscript, data interpretation and discussion.

Additional Information

Supplementary Information accompanies this letter at https://www.geochemicalperspectivesletters.org/article2126.

Cite this letter as: Hatton, J.E., Hendry, K.R., Hawkings, J.R., Wadham, J.L., Benning, L.G., Blukis, R., Roddatis, V., Ng, H.C., Wang, T. (2021) Physical weathering by glaciers enhances silicon mobilisation and isotopic fractionation. *Geochem. Persp. Let.* 19, 7–12.

References

Basile-Doelsch, I., Meunier, J.D., Parron, C. (2005) Another continental pool in the terrestrial silicon cycle. *Nature* 433, 399–402.

Blackburn, T., Siman-Tov, S., Coble, M.A., Stock, G.M., Brodsky, E.E., Hallet, B. (2019) Composition and formation age of amorphous silica coating glacially polished surfaces. *Geology* 47, 347–350.

Casey, W.H., Westrich, H.R., Banfield, J.F., Ferruzzi, G., Arnold, G.W. (1993) Leaching and reconstructing at the surface of dissolving chain-silicate minerals. *Nature* 366, 253–256.

Demarest, M.S., Brzezinski, M.A., Beucher, C.P. (2009) Fractionation of silicon isotopes during biogenic silica dissolution. *Geochimica et Cosmochimica Acta* 73, 5572–5583.

Frings, P.J., Clymans, W., Fontorbe, G., De La Rocha, C., Conley, D.J. (2016) The continental Si cycle and its impact on the ocean Si isotope budget. *Chemical Geology* 425, 12–36.

Hatton, J.E., Hendry, K.R., Hawkings, J.R., Wadham, J.L., Kohler, T.J., Stibal, M., Beaton, A.D., Bagshaw, E.A., Telling, J. (2019a) Investigation of subglacial weathering under the Greenland Ice Sheet using silicon isotopes. *Geochimica et Cosmochimica Acta* 247, 191–206.

Hatton, J.E., Hendry, K.R., Hawkings, J.R., Wadham, J.L., Opfergelt, S., Kohler, T.J., Yde, J.C., Stibal, M., Zarsky, J.D. (2019b) Silicon Isotopes in Arctic and sub-Arctic Glacial Meltwaters: The Role of Subglacial Weathering in the Silicon Cycle. *Proceedings of the Royal Society A.* 475, 20190098.

Hawkings, J.R., Wadham, J.L., Tranter, M., Lawson, E., Sole, A., Cowton, T., Tedstone, A.J., Bartholomew, I., Nienow, P., Chandler, D., Telling, J. (2015) The effect of warming climate on nutrient and solute export from the Greenland Ice Sheet. *Geochemical Perspectives Letters* 1, 94–104.

Hawkings, J.R., Wadham, J.L., Benning, L.G., Hendry, K.R., Tranter, M., Tedstone, A., Nienow, P., Raiswell, R. (2017) Ice sheets as a missing source of silica to the polar oceans. *Nature Communications* 8, 14198.

Hawkings, J.R., Hatton, J.E., Hendry, K.R., de Souza, G.F., Wadham, J.L., Ivanovic, R., Kohler, T.J., Stibal, M., Beaton, A., Lamarche-Gagnon, G., Tedstone, A., Hain, M.P., Bagshaw, E., Pike, J., Tranter, M. (2018) The silicon cycle impacted by past ice sheets. *Nature Communications* 9, 3210.

Hellmann, R., Wirth, R., Daval, D., Barnes, J.-P., Penisson, J.-M., Tisserand, D., Epicier, T., Florin, B., Hervig, R.L. (2012) Unifying natural and laboratory chemical weathering with interfacial dissolution–reprecipitation: A study based on the nanometer-scale chemistry of fluid–silicate interfaces. *Chemical Geology* 294–295, 203–216.

Hendry, K.R., Huvenne, V.A.I., Robinson, L.F., Annett, A., Badger, M., Jacobel, A.W., Ng, H.C., Opher, J., Pickering, R.A., Taylor, M.L., Bates, S.L., Cooper, A., Cushman, G.G., Goodwin, C., Hoy, S., Rowland, G., Samperiz, A., Williams, J.A., Achterberg, E.P., Arrowsmith, C., Alexander Brearley, J., Henley, S.F., Krause, J.W., Leng, M.J., Li, T., McManus, J.F., Meredith, M.P., Perkins, R., Woodward, E.M.S. (2019) The biogeochemical impact of glacial meltwater from Southwest Greenland. *Progress in Oceanography* 176, 102126.

Michaud, A.B., Skidmore, M.L., Mitchell, A.C., Vick-Majors, T.J., Barbante, C., Turetta, C., vanGelder, W., Priscu, J.C. (2016) Solute sources and geochemical processes in Subglacial Lake Whillans, West Antarctica. *Geology* 44, 347–350.

Opfergelt, S., Burton, K.W., Pogge von Strandmann, P.A.E., Gislason, S.R., Halliday, A.N. (2013) Riverine silicon isotope variations in glaciated basaltic terrains: Implications for the Si delivery to the ocean over glacial–interglacial intervals. *Earth and Planetary Science Letters* 369–370, 211–219.

Sharp, M., Tranter, M. (2017) Glacier Biogeochemistry. *Geochemical Perspectives* 6, 173–174.

Telling, J., Boyd, E.S., Bone, N., Jones, E.L., Tranter, M., MacFarlane, J.W., Martin, P.G., Wadham, J.L., Lamarche-Gagnon, G., Skidmore, M.L., Hamilton, T.L., Hill, E., Jackson, M., Hodgson, D.A. (2015) Rock comminution as a source of hydrogen for subglacial ecosystems. *Nature Geoscience* 8, 851–855.

Wadham, J.L., Tranter, M., Skidmore, M., Hodson, A.J., Priscu, J., Lyons, W.B., Sharp, M., Wynn, P., Jackson, M. (2010) Biogeochemical weathering under ice: Size matters. *Global Biogeochemical Cycles* 24, GB3025.

Yund, R.A., Blanpied, M.L., Tullis, T.E., Weeks, J.D. (1990) Amorphous material in high strain experimental fault gouges. *Journal of Geophysical Research* 95, 15589–15602.

Ziegler, K., Chadwick, O.A., Brzezinski, M.A., Kelly, E.F. (2005) Natural variations of δ^{30}Si ratios during progressive basalt weathering, Hawaiian Islands. *Geochimica et Cosmochimica Acta* 69, 4597–4610.

Physical weathering by glaciers enhances silicon mobilisation and isotopic fractionation

J.E. Hatton, K.R. Hendry, J.R. Hawkings, J.L. Wadham, L.G. Benning, R. Blukis, V. Roddatis, H.C. Ng, T. Wang.

Supplementary Information

The Supplementary Information includes:

Sample Description

Rock debris (ranging from >2 mm finely ground material to up to ~5 cm diameter rock pieces), was collected from the proglacial environment of Leverett Glacier, south-west Greenland, approximately 1 km from the glacier portal (Fig. S-2). Leverett Glacier overlays bedrock that is considered relatively representative of much of the area covered by the Greenland Ice Sheet (GrIS) and once covered by the Fennoscandian ice sheet (Bouysse, 2014; Hawkings *et al.*, 2018). The lithology at Leverett Glacier is dominated by Precambrian Shield granite and gneiss (Lawson *et al.*, 2014). We conducted X-ray diffraction analysis of the samples prior to reaction to assess the mineralogical composition (Fig. S-1), with results showing 47 % albite rich plagioclase, 31 % quartz, 13 % K-feldspar, 6 % Hornblende and 3 % sheet silicates. These results agree well with previous analysis of the area (Hindshaw *et al.*, 2014), thus providing evidence that the material used in these experiments is representative of the region. In addition, Leverett Glacier is one of the most studied outflow glaciers of the GrIS (Bartholomew *et al.*, 2011; Cowton *et al.*, 2012; Clason *et al.*, 2015; Beaton *et al.*, 2017; Hawkings *et al.*, 2017; Kohler *et al.*, 2017; Hawkings *et al.*, 2018), allowing experimental data to be compared to numerous years of field data, helping to contextualise the experimental results.

Detailed Experimental Set-Up

Proglacial till material collected at Leverett Glacier was briefly rinsed with Ultra-pure water (18.2 MW cm, Milli-Q, Millipore®) and air dried in a laminar flow hood in preparation for crushing. First, rocks were placed in several, thick

polyethene bags and crushed using a sledgehammer and metal plate. The resulting fragments were then passed through mechanical jaws to reduce the particle size further. The sample was then sieved and the <2 mm size fraction was retained for milling. Samples were dry milled using an agate ball mill in a Fritsch Planetary Mono Mill Pulverisette at 500 rpm for either 2 or 30 minutes (T2 and T30), to mimic two different erosion intensities.

After milling, samples were prepared in triplicate for each time point by adding 2.00 ± 0.01 g of milled sediment to 50 mL centrifuge tubes, cleaned by soaking in 2M HCl for 24 hours then ultra-pure (MQ) water for 24 hours. Experiments were started with the addition of 40 mL MQ water to the milled rock material. A sediment: water ratio of 50 g L^{-1} was used in all dissolution experiments, as this is sufficiently high to mimic rock-water ratios in the subglacial environment, when considering the potentially high erosion rates calculated from suspended sediment fluxes at LG. Samples were kept at 4 °C on a shaker at 100 rpm in the dark for the duration of the experiment. At pre-determined timepoints (4, 24, 48, 168, 336 and 720 hours) experiments were terminated by centrifuging the tubes and filtering the supernatant through 0.22 μm Sartorius™ Minisart™ High Flow PES membrane filters. The filtrate was stored at 4 °C until analysis and the sediments were allowed to air dry in a laminar flow hood (IS05). Once dry, the sediment was partitioned for solid state analysis or re-crushing. Re-crushing was completed using a pestle and mortar and the experiment outlined above was repeated by reacting the solids for 4, 48 and 720 hours again with MQ water.

Control experiments were set up to establish DSi and ASi concentrations of starting material prior to milling. Here, unmilled material was added to centrifuge tubes and then 40ml of MQ water was added. The control experiments were kept under the same conditions as the milled experiments, as outlined above. However, it was not possible to keep the sample weight of the control experiments at 2.00 ± 0.01 g, due to the large size of some un-milled material. Despite the greater sediment to water ratios, Table S-5 shows that DSi concentrations from unmilled samples were <3 % of the total DSi content from milled experiments. These values have been blanked corrected using an average for the full experimental blank (0.33 μM, n = 3), where MQ water was added to cleaned centrifuge tubes and left on a shaker at 4 °C for 720 hours. Control ASi concentrations were calculated from unmilled starting material that was either unreacted with MQ water or reacted with MQ water for up to 168 hours (from the DSi control experiments). ASi extractions were completed using the same methodology as outlined below, with a weak alkaline leach for up to 5 hours. Table S-6 shows that the ASi extracted from unmilled starting material is <7 % of the T2 experiment sets and <2 % of the T30 experiment sets. The range of ASi concentrations from the control experiments (below limit of detection to 0.04 wt. %) highlights the heterogenous nature of the starting material, with larger rocks (with a smaller specific surface area) resulting in the lowest ASi concentrations.

Agate Mill Tests

The milling methodology employed follows procedures routinely carried out in the silicon isotope community (*i.e.* to establish bulk Si isotopic composition of solid materials) and previous testing has been conducted to show that agate ball milling does not result in any sample contamination with respect to Si (Savage *et al.,* 2011). However, we recognise that previous tests did not mill material for 30 minutes, so we completed some additional tests to ensure this increased milling did not result in any contamination from the agate ball mill.

Samples were milled in a Retsch Mixer Mill MM 400, using both steel and agate mills for up to 30 minutes (stopping at 2, 4, 10, 20 and 30 minutes to collect sub-samples for analysis). Samples were milled at 8.33 Hz and each sub-sample was mixed with 10 wt. % CeO$_2$ before XRD analysis. This allowed us to compare any differences in ASi concentration between the agate and steel mills and assess any potential contamination. Figure S-6 shows no significant differences in ASi concentrations for all timepoints between the steel and agate mills, during XRD analysis.

Laboratory Analyses

Water samples were stored refrigerated prior to analysis for major ion concentrations, DSi concentrations and $\delta^{30}Si_{DSi}$. Major ion concentrations were analysed by capillary ion chromatography using a Thermo Scientific Dionex ICS-5000+, as described previously by Hawkings *et al.* (2015). DSi concentrations were analysed spectrophotometrically using Flow Injection Analysis, as described by Hatton *et al.* (2019) and Hawkings *et al.* (2018).

Once dry, the solid phase was partitioned for alkaline extraction to determine ASi concentration. ASi concentrations were determined using an alkaline 0.1 M Na_2CO_3 extraction, modified from Demaster (1981) and used previously for riverine suspended sediments (Hatton *et al.*, 2019).

Silicon Isotope Composition

Samples were measured for dissolved, amorphous and bulk ($\delta^{30}Si_{DSi}$, $\delta^{30}Si_{ASi}$, and $\delta^{30}Si_{bulk}$ respectively) silicon isotope composition using a Thermo Scientific Neptune Plus High-Resolution MC-IPC-MS in the Bristol Isotope Group Laboratories at the University of Bristol. Methods are detailed previously in Hatton *et al.* (2019) and Hawkings *et al.* (2018). Briefly, measurements of ^{28}Si, ^{29}Si and ^{30}Si were made in triplicate in wet plasma mode. Standard-sample-standard bracketing was employed and all samples and standards were doped with 100 µL of 10 ppm Mg solution to correct for instrumental mass bias (Cardinal *et al.*, 2010) and 50 µL H_2SO_4 (0.01 M) to remove any anionic mass bias matrix effects (Hughes *et al.*, 2011). Results are reported as $\delta^{30}Si$, which is calculated based on the deviation from the ratio of $^{28}Si/^{30}Si$ from the bracketing standard:

$$\delta^{30}Si = \left[\frac{\left(\frac{^{30}Si}{^{28}Si}\right)sample}{\left(\frac{^{30}Si}{^{28}Si}\right)NBS28} - 1 \right] x\ 1000$$

Eq. S-1

A three isotope plot (Fig. S-6) demonstrates that samples and standards measured for this study display mass dependent fractionation, with a gradient of 0.5119 (Reynolds *et al.*, 2007). Reference standards LMG ($\delta^{30}Si$ = -3.42 ± 0.13 ‰, 2 s.d., n = 13) and Diatomite ($\delta^{30}Si$ = +1.22 ± 0.14 ‰, 2 s.d., n = 24) measured alongside samples show good agreement with published values (Reynolds *et al.*, 2007; Hendry *et al.*, 2011). Long term reproducibility of these standards measured between 2015–2020 also show good agreement with published values (LMG: -3.44 ± 0.07 ‰ 2 s.d., n = 138; Diatomite: +1.22 ± 0.07 ‰, 2 s.d., n = 99).

Grainsize Analysis

Grain size was measured using a Malvern Mastersizer 3000 system, that can measure particle sizes between 0.02 µm and 2000 µm. Ultra pure Milli-Q water was used as the dispersion media and an obscurity between 5–15 % (stability ± 0.1 %) was ensured. Internal precision (average 2 s.d. = 1.2 %) was calculated from five measurements of each sample and selected samples were replicated in triplicate to assess external reproducibility (average 2 s.d. = 7 %). Analysis showed that re-crushing the solid phase using a pestle and mortar resulted in consistent grainsize distributions within the T2 and T30 samples.

High resolution transmission electron microscopy (HR-TEM)

Initial, milled and reacted samples were imaged and spectrally analysed using a high-resolution transmission electron microscope (HR-TEM, FEI Tecnai TF20 at 200 kV). A small amount of sample (<10 mg) was dispersed for 10 minutes in ethanol in a microcentrifuge tube using an ultrasonic bath. A 2–4 µL drop of the

dispersed solution was pipetted onto a holey carbon support grid and allowed to dry. Images and analyses were collected on a TECNAI F20 XTWIN TEM operated at 200 kV with a field emission gun electron source, a Gatan Imaging Filter (GIF) Tridiem™, and an EDAX X-ray analyser.

X-Ray Scattering Analysis

Reduced pair distribution function (G(r)) analysis. The changes induced due to the milling and reaction with water were analysed using G(r) analysis calculated from measured total X-ray scattering patterns. For these measurements the powdered samples where loaded in 0.5 mm diameter glass capillaries (Hilgenberg 4007405). X-ray scattering patterns were measured using a STOE STADI P instrument with an Ag X-ray source (λ = 0.55941 Å), curved Ge (111) monochromator and DECTRIS MYTHEN2 detector. Measurements were performed in a Debye-Scherrer geometry for a Q up to 20.52 $Å^{-1}$ and with an angular resolution of 0.015°. Average measurement time per sample was 4 days with longer measurement time scaled for the high Q regions. The scattering data was processed using PDFgetX2 software (Qiu *et al.*, 2004). The raw X-ray scattering pattern was corrected for sample geometry, capillary and air scattering background, absorption, radiation polarisation, Compton scattering and multiple (2nd) scattering to obtain the correct structure factor S(Q) (Egami and Billinge, 2003). For absorption and atomic form factor corrections, we also determined the average chemical composition of the samples (64 at. % O, 21 at. % Si, 7 at. % Al, 4 at. % Na, 2 at. % K, 1 at. % Ca, 0.7 at. % Fe, 0.4 at. % Mg, 0.2 at. % Ti; ±5 at. % error can be assumed for all elements) using a scanning electron microscope (FEI Quanta 3D, run at 20 keV) equipped with an EDAX EDS detector (EDAX Loctane ELECT PLUS). In all cases a large area of the sample was mapped to determine elemental contributions, and the composition was then assumed to be the same across the whole sample.

Mineralogical analysis. Mineralogical changes and amorphous content of the samples was measured from diffractions patterns measured using a STOE STADI P instrument with a Cu X-ray source (λ = 1.5406 Å), curved Ge (111) monochromator and DECTRIS MYTHEN2 detector in Debye-Scherrer geometry. The powdered samples were mixed with approximately 10 wt. % of precisely measured amount of CeO_2 and loaded in 0.5 mm diameter glass capillaries (Hilgenberg 4007405). The scattering pattern was measured in range of 0–84° 2θ with a resolution of 0.015° and the measurement time of 6 hours per sample (10,700 seconds per degree 2θ). The instrument profile was calibrated using a NIST Si standard. For Rietveld analysis mineral reference CIF files were obtained from COD database. The background was fitted with an empirical polynomial function. The mineral cell parameters, grain size, microstrain and solid solution composition, where appropriate, were allowed to vary during the refinement. The accuracy of the refinement is estimated to be within 2–5 wt. %.

Supplementary Tables

Table S-1   Summary of results from original batch experiments. Each batch included 3 replicate samples, with the standard deviation between these samples shown in square brackets (where available). Isotopic external error is the variability in triplicate measurements of a single sample (2 s.d.).

Batch	Milling Time (mins)	Incubation Time (hours)	DSi (μM) [s.d., n = 3]	$\delta^{30}Si_{DSi}$ (‰) [s.d., n = 3]	$\delta^{30}Si_{DSi}$ Ext. error (‰), 2 s.d., n = 3	ASi (%) [s.d., n = 3]	$\delta^{30}Si_{ASi}$ (‰)	$\delta^{30}Si_{ASi}$ Ext. error (‰) 2 s.d., n = 3	Divalent: Monovalent (D:M) Ion ratio (μM) [s.d., n = 3]
T2-4	2	4	13.04 [0.77]	-1.97 [0.17]	0.04	0.08 [0.02]	-0.18	0.09	0.13 [0.01]
T2-24	2	24	18.58 [0.86]	-0.95	0.13	0.10	-0.20	0.08	0.09 [0.01]
T2-48	2	48	31.49 [0.22]	-0.80	0.09	0.30 [0.13]	-0.24	0.05	0.12 [0.01]
T2-120	2	120	24.70 [2.81]	-0.48	0.12	0.10	-0.25	0.08	0.12 [0.01]
T2-336	2	336	31.49 [1.03]	-0.98 [0.08]	0.08	0.15	-0.29	0.01	0.12 [0.01]
T2-720	2	720	51.17 [4.29]	-0.13	0.15	0.05	-0.15	0.10	0.16 [0.01]
T30-4	30	4	46.13 [2.23]	-1.56	0.09	0.67	-0.17	0.02	0.03 [<0.01]
T30-24	30	24	57.61 [0.97]	-0.62	0.04	0.53 [0.11]	-0.12	0.02	0.02 [<0.01]
T30-48	30	48	58.06 [1.21]	-0.53 [0.02]	0.06	0.48	-0.10	0.11	0.03 [<0.01]
T30-120	30	120	73.47 [2.25]	-0.33	0.01	0.98 [0.09]	-0.23	0.03	0.03 [<0.01]
T30-336	30	336	89.01 [3.38]	-0.71 [0.03]	0.07	1.45	-0.24	0.09	0.02 [<0.01]
T30-720	30	720	81.12 [5.28]	-0.07	0.01	0.62 [0.13]	-0.21	0.09	0.04 [<0.01]

Table S-2   Summary of results from batch experiments after re-crushing. Each batch included triplicate samples, with the standard deviation between these samples shown in square brackets.

Batch	Original Milling Time (mins)	Secondary Incubation Time (hours)	Average DSi (μM) [s.d., n = 3]	$\delta^{30}Si_{DSi}$ (‰) [s.d., n = 3]	ASi (%) [s.d., n = 3]	$\delta^{30}Si_{ASi}$ (‰) [s.d., n = 3]	Average D:M (μM) [s.d., n = 3]
T2-RC4	2	4	11.06 [1.34]	-1.14 [0.12]	0.15 [0.02]	-0.25 [0.02]	0.04 [0.03]
T2-RC48	2	48	21.62 [1.01]	-1.05 [0.05]	0.08 [0.05]	-0.16 [0.02]	0.02 [0.01]
T2-RC720	2	720	49.51 [2.25]	-0.17 [0.06]	0.21 [0.04]	-0.30 [0.02]	0.08 [0.05]
T30-RC4	30	4	25.25 [2.15]	-0.99 [0.12]	0.98 [0.02]	-0.19 [0.08]	0.01 [<0.01]
T30-RC48	30	48	48.99 [2.33]	-0.59 [0.10]	0.95 [0.04]	-0.22 [0.06]	<0.01 [<0.01]
T30-RC720	30	720	89.01 [3.10]	-0.01 [0.03]	0.66 [0.28]	-0.22 [0.07]	0.01 [<0.01]

Table S-3 Molar major ion concentrations from batch experiments. Each batch included triplicate samples, with the standard deviation between these samples shown in square brackets.

Batch	Milling Time (mins)	Incubation Time (hrs)	Average Ca^{2+} (µM) [s.d., n = 3]	Average Mg^{2+} (µM) [s.d., n = 3]	Average Na^+ (µM) [s.d., n = 3]	Average K^+ (µM) [s.d., n = 3]	Divalent: Monovalent (D:M) Ion ratio (µM) [s.d., n = 3]
T2-4	2	4	4.33 [1.06]	8.85 [1.49]	71.67 [10.51]	40.36 [6.85]	0.13 [0.01]
T2-24	2	24	3.94 [0.62]	7.09 [0.38]	75.40 [3.41]	52.35 [1.38]	0.09 [0.01]
T2-48	2	48	6.91 [1.88]	9.02 [0.62]	77.92 [0.07]	55.11 [0.19]	0.12 [0.01]
T2-120	2	120	6.11 [1.00]	9.64 [0.91]	87.63 [4.42]	53.51 [7.53]	0.12 [0.01]
T2-336	2	336	5.23 [0.62]	11.33 [2.30]	107.29 [0.12]	55.62 [0.89]	0.12 [0.01]
T2-720	2	720	12.73 [1.51]	17.66 [2.71]	113.45 [7.04]	78.50 [4.57]	0.16 [0.01]
T30-4	30	4	384.27 [11.92]	206.85 [6.66]	13.11 [0.822]	2.13 [0.52]	0.03 [<0.01]
T30-24	30	24	334.21 [5.13]	172.32 [1.71]	9.83 [0.99]	1.50 [0.37]	0.02 [<0.01]
T30-48	30	48	340.89 [4.99]	173.32 [1.71]	11.60 [0.34]	2.42 [0.26]	0.03 [<0.01]
T30-120	30	120	401.05 [13.05]	192.98 [7.22]	13.02 [0.48]	3.02 [0.29]	0.03 [<0.01]
T30-336	30	336	548.41 [12.45]	238.69 [11.03]	11.72 [1.08]	1.07 [1.27]	0.02 [<0.01]
T30-720	30	720	514.89 [6.86]	223.84 [5.70]	14.84 [1.95]	3.35 [0.80]	0.04 [<0.01]

Table S-4 Molar major ion concentrations from batch experiments. Each batch included triplicate samples, with the standard deviation between these samples shown in square brackets.

Batch	Original Milling Time (mins)	Secondary Incubation Time (hours)	Average Ca^{2+} (μM) [s.d., n = 3]	Average Mg^{2+} (μM) [s.d., n = 3]	Average Na^+ (μM) [s.d., n = 3]	Average K^+ (μM) [s.d., n = 3]	Average D:M (μM) [s.d., n = 3]
T2-RC4	2	4	1.82 [1.61]	2.87 [1.53]	77.13 [4.67]	44.37 [6.28]	0.04 [0.03]
T2-RC48	2	48	0.64 [0.45]	2.52 [2.25]	79.19 [11.35]	39.78 [1.07]	0.02 [0.01]
T2-RC720	2	720	4.35 [3.62]	7.07 [4.64]	103.89 [20.59]	52.48 [6.27]	0.08 [0.05]
T30-RC4	30	4	0.34 [0.25]	1.19 [0.37]	220.15 [21.63]	69.97 [13.61]	0.01 [<0.01]
T30-RC48	30	48	<LOD	1.37 [0.81]	281.36 [49.38]	85.96 [6.34]	<0.01 [<0.01]
T30-RC720	30	720	<LOD	2.03 [0.47]	262.58 [19.03]	99.25 [8.61]	0.01 [<0.01]

Table S-5 Summary of DSi concentrations results from unmilled control experiments. <LoD = Below Limit of Detection (FIA LoD = 10 ppb). Unmilled rock debris was reacted with MQ-grade water for 4, 24, 48 and 168 hours.

Sample	Incubation Time (hrs)	Average DSi (μM) (n = 3)	DSi (μM) range	Total of [DSi] measured from T2 experiments at same timepoint (%)	Total of [DSi] measured from T2 experiments at same timepoint (%)
Unmilled Control – 4	4	0.09	0.08–0.12	0.71	0.20
Unmilled Control -24	24	0.25	0.15–0.43	1.30	0.43
Unmilled Control -48	48	0.44	0.18–0.88	2.36	0.75
Unmilled Control - 168	168	0.58	0.46–0.77	2.37	0.80

Table S-6 Summary of ASi concentrations results from unmilled control experiments. ASi concentrations measured after Na_2CO_3 extraction of unmilled rock samples. <LoD = Below Limit of Detection (FIA LoD = 10 ppb).

| Sample	Incubation Time (hrs)	Sample weight (g)	ASi (wt. %)
ASi Control 1	Unreacted	0.32	0.014
ASi Control 2	Unreacted	11.44	0.002
ASi Control 3	Unreacted	3.78	0.004
ASi Control 4	Unreacted	0.51	0.022
ASi Control 5	4	7.90	0.001
ASi Control 6	24	0.71	0.010
ASi Control 7	48	0.16	0.035
ASi Control 8	168	0.50	<LOD
Average	-	-	0.011
Total of [ASi] measured from T2 (%)	-	-	6.41
Total of [ASi] measured from T30 (%)	-	-	1.68

Supplementary Figures
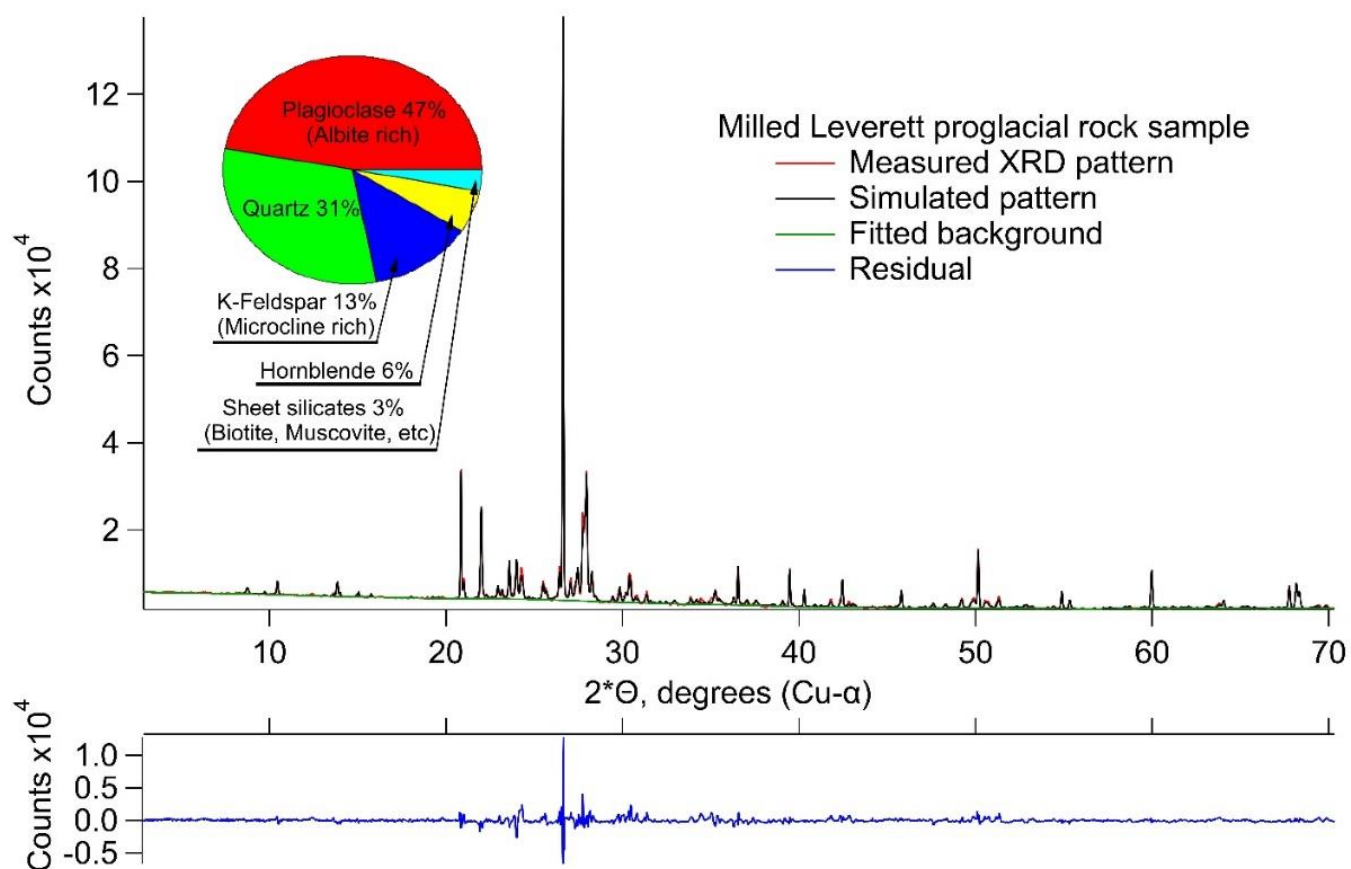
Figure S-1   Mineral composition of proglacial rock debris derived from X-ray diffraction analyses. Shown are measured and Rietveld refined, simulated patterns as well as residual (see y-axis difference).
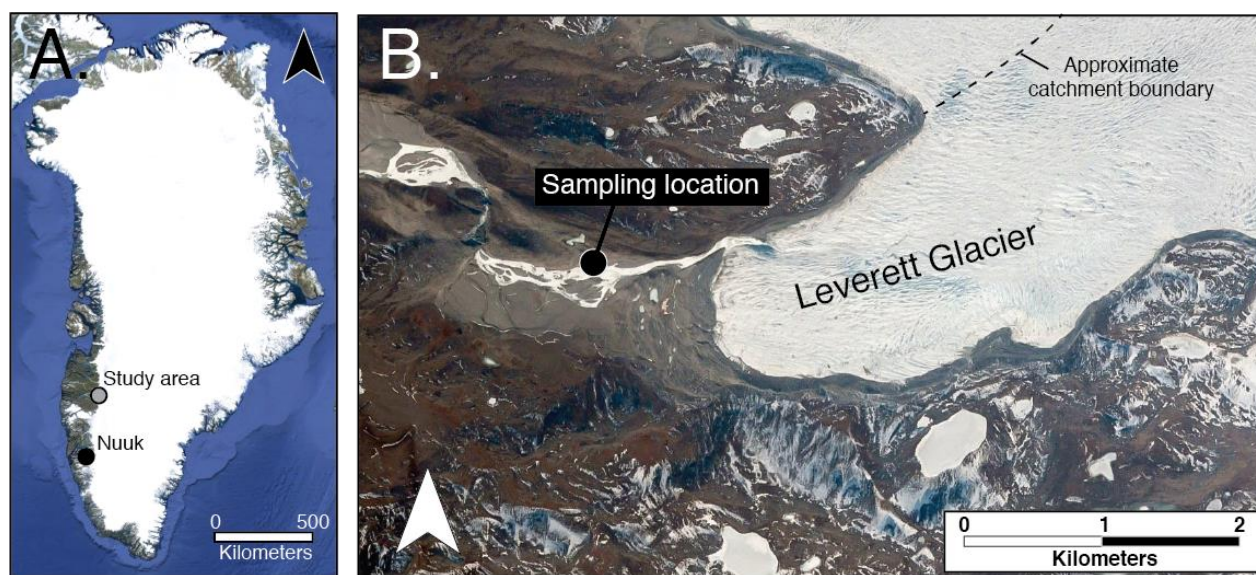
Figure S-2   Map of Leverett Glacier, in the context of the Greenland Ice Sheet. **(a)** Landsat US Geological Survey, *via* Google), with the sample collection location shown by the black circle in **(b)** (DigitalGlobe, *via* Google), as published by Hawkings *et al.* (2018).
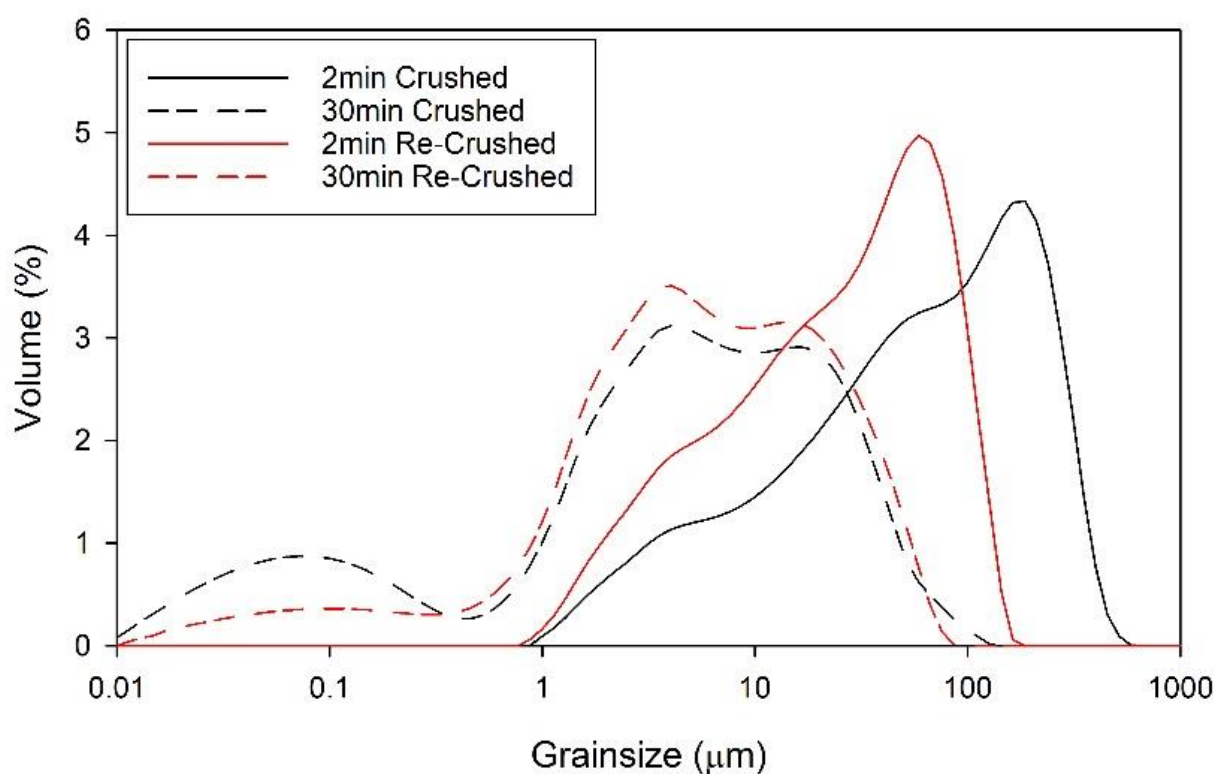

Figure S-3   Grainsize distribution of T2 and T30 sediment, for primary and secondary crushing experiments. Black lines represent primary crushing experiments and red lines represent secondary crushing experiments, with solid lines showing T2 and dashed lines showing T30. Data is an average of 3 external replicate measurements, internally measured 5 times.
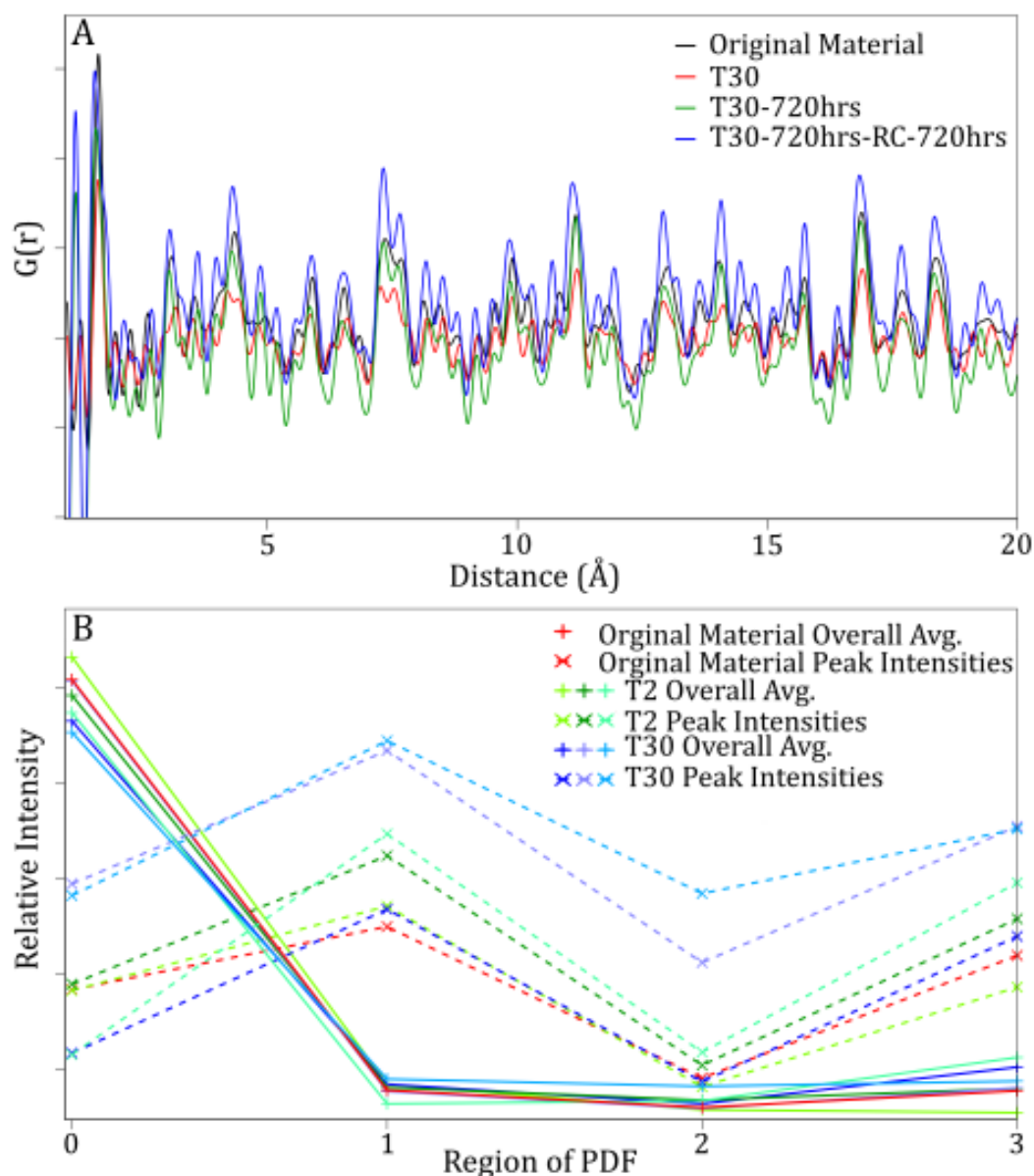
Figure S-4 **(a)** Reduced pair distribution functions G(r) of samples T30 (milled and reacted) compared to the starting material before milling. **(b)** Plot of empirical crystallinity proxies. Solid lines (overall Avg.) correspond to integrated intensity under the PDF curve squared in 1st, 2nd, 3rd, 4th quarter of the PDF normalised by the maximum intensity of Si-O correlation peak (at 1.6Å). Dashed lines correspond to two highest peak intensity in each quarter sum normalised by the intensity of Si-O correlation peak. All samples follow the same crystallinity pattern, within error.
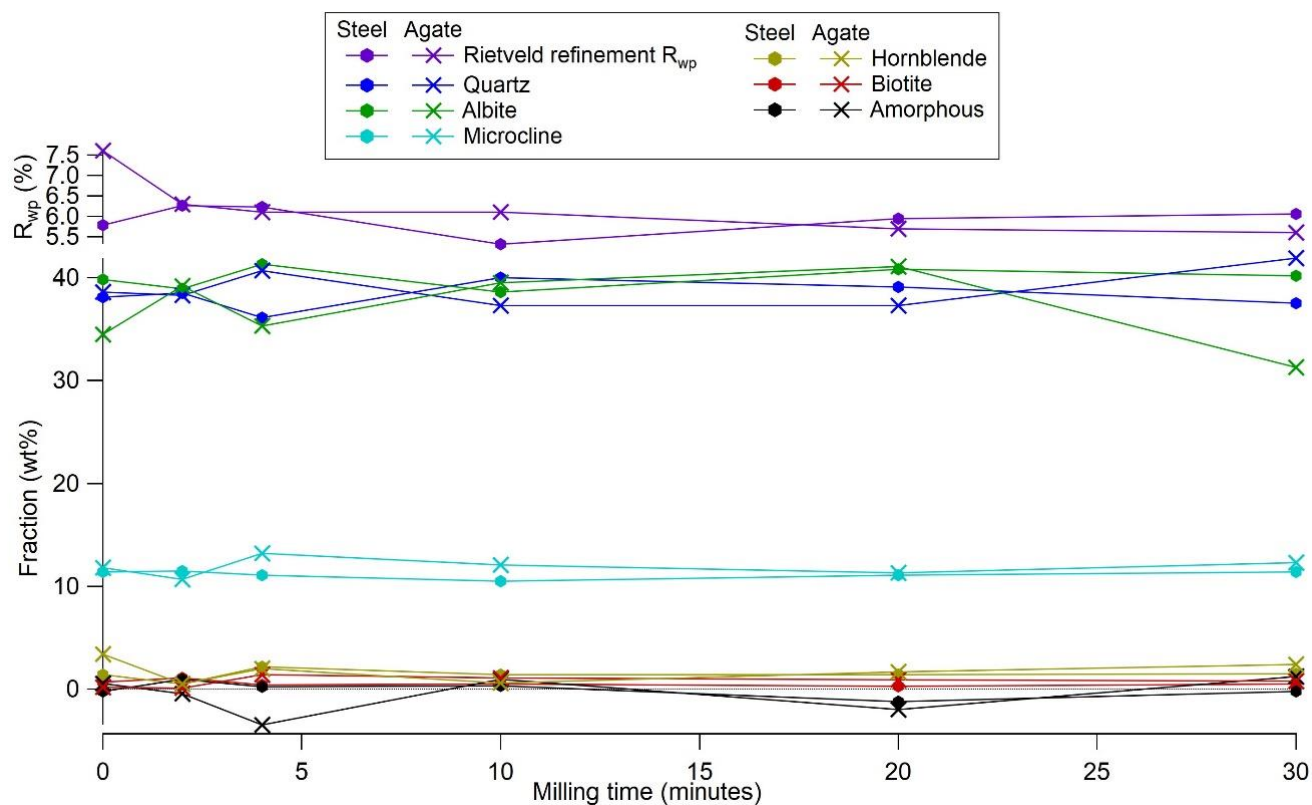
Figure S-5 Mineralogical compositions of the samples milled with agate and steel mill for different duration of time. A slightly increased R_{wp} of the agate milled t = 0 min sample is mostly likely caused by slightly coarser grain size (Fig. S-3) that has resulted in the sample measured not having completely uniform grain orientation averaging resulting in increased preferential orientation.
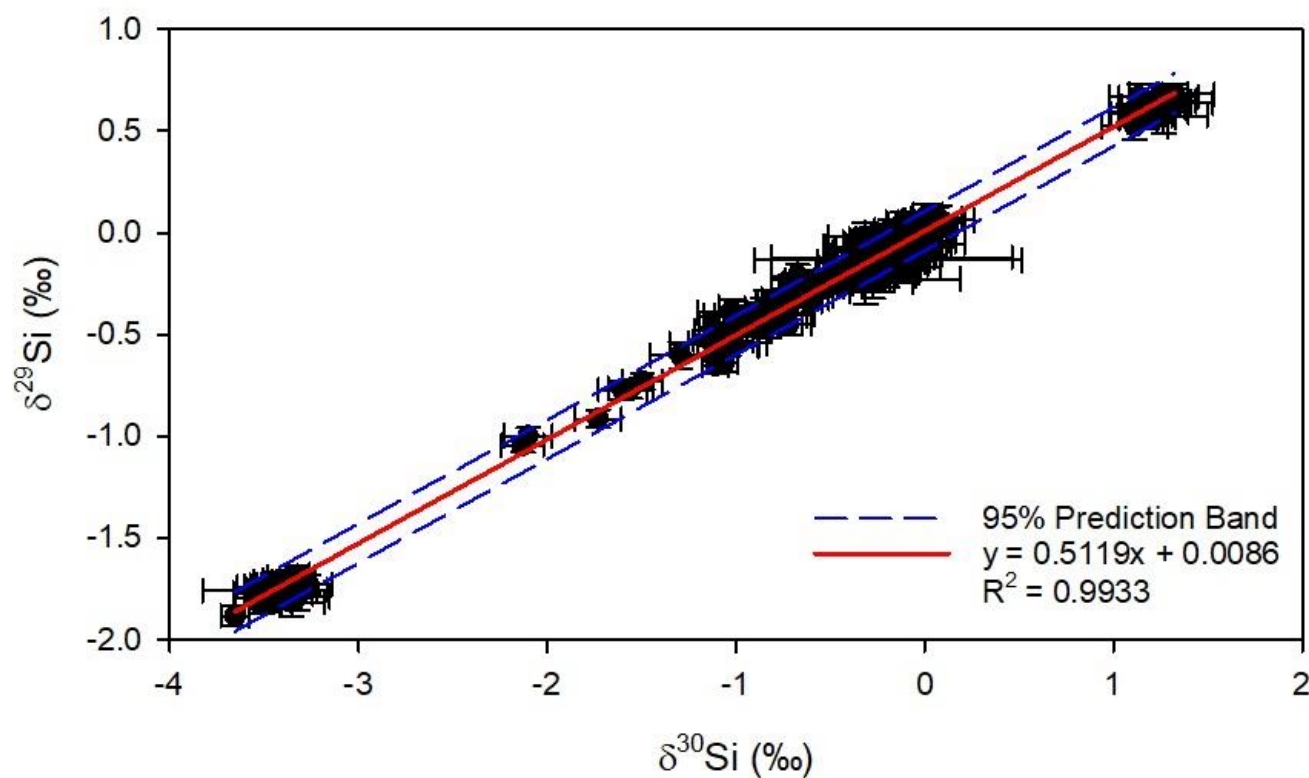
Figure S-6   Three isotope plot of all measurements carried out during this study. Plot showing $\delta^{29}Si$ versus $\delta^{30}Si$ of samples and standards, with a red regression line of 0.512 ± 0.009 ‰. Blue dashed lines indicate the 95 % prediction intervals and error bars are the machine internal errors.

Supplementary Information References

Bartholomew, I., Nienow, P., Sole, A., Mair, D., Cowton, T., Palmer, S., Wadham, J. (2011) Supraglacial forcing of subglacial drainage in the ablation zone of the Greenland ice sheet. *Geophysical Research Letters* 38, L08502.

Beaton, A.D., Wadham, J.L., Hawkings, J., Bagshaw, E.A., Lamarche-Gagnon, G., Mowlem, M.C., Tranter, M. (2017) High-Resolution in Situ Measurement of Nitrate in Runoff from the Greenland Ice Sheet. *Environmental Science & Technology* 51, 12518-12527.

Bouysse, P. (2014) *Geological Map of the World at 1:35 000 000*. Third Edition, CCGM-CGMW, Paris.

Cardinal, D., Gaillardet, J., Hughes, H.J., Opfergelt, S., André, L. (2010) Contrasting silicon isotope signatures in rivers from the Congo Basin and the specific behaviour of organic-rich waters. *Geophysical Research Letters* 37, L12403.

Clason, C.C., Mair, D.W.F., Nienow, P.W., Bartholomew, I.D., Sole, A., Palmer, S., Schwanghart, W. (2015) Modelling the transfer of supraglacial meltwater to the bed of Leverett Glacier, Southwest Greenland. *The Cryosphere* 9, 123-138.

Cowton, T., Nienow, P., Bartholomew, I., Sole, A., Mair, D. (2012) Rapid erosion beneath the Greenland ice sheet. *Geology* 40, 343-346.

DeMaster, J.D. (1981) The supply and accumulation of silica in the marine environment. *Geochimica et Cosmochimica Acta* 45, 1715-1732.

Egami, T., Billinge, S.J.L. (2003) *Underneath the Bragg Peaks*. First Edition, Pergamon, London.

Hatton, J.E., Hendry, K.R., Hawkings, J.R., Wadham, J.L., Kohler, T.J., Stibal, M., Beaton, A.D., Bagshaw, E.A., Telling, J. (2019) Investigation of subglacial weathering under the Greenland Ice Sheet using silicon isotopes. *Geochimica et Cosmochimica Acta* 247, 191-206.

Hawkings, J.R., Wadham, J.L., Tranter, M., Lawson, E., Sole, A., Cowton, T., Tedstone, A.J., Bartholomew, I., Nienow, P., Chandler, D., Telling, J. (2015) The effect of warming climate on nutrient and solute export from the Greenland Ice Sheet. *Geochemical Perspectives Letters* 1, 94-104.

Hawkings, J.R., Wadham, J.L., Benning, L.G., Hendry, K.R., Tranter, M., Tedstone, A., Nienow, P., Raiswell, R. (2017) Ice sheets as a missing source of silica to the polar oceans. *Nature Communications* 8, 14198.

Hawkings, J.R., Hatton, J.E., Hendry, K.R., de Souza, G.F., Wadham, J.L., Ivanovic, R., Kohler, T.J., Stibal, M., Beaton, A., Lamarche-Gagnon, G., Tedstone, A., Hain, M.P., Bagshaw, E., Pike, J., Tranter, M. (2018) The silicon cycle impacted by past ice sheets. *Nature Communications* 9, 3210.

Hendry, K.R., Leng, M.J., Robinson, L.F., Sloane, H.J., Blusztjan, J., Rickaby, R.E.M., Georg, R.B., Halliday, A.N. (2011) Silicon isotopes in Antarctic sponges: an interlaboratory comparison. *Antarctic Science* 23, 34-42.

Hindshaw, R.S., Rickli, J., Leuthold, J., Wadham, J., Bourdon, B. (2014) Identifying weathering sources and processes in an outlet glacier of the Greenland Ice Sheet using Ca and Sr isotope ratios. *Geochimica et Cosmochimica Acta* 145, 50-71.

Hughes, H.J., Delvigne, C., Korntheuer, M., de Jong, J., André, L., Cardinal, D. (2011) Controlling the mass bias introduced by anionic and organic matrices in silicon isotopic measurements by MC-ICP-MS. *Journal of Analytical Atomic Spectrometry* 26, 1892.

Kohler, T.J., Žárský, J.D., Yde, J.C., Lamarche-Gagnon, G., Hawkings, J.R., Tedstone, A.J., Wadham, J.L., Box, J.E., Beaton, A.D., Stibal, M. (2017) Carbon dating reveals a seasonal progression in the source of particulate organic carbon exported from the Greenland Ice Sheet. *Geophysical Research Letters* 44, 6209-6217.

Lawson, E.C., Wadham, J.L., Tranter, M., Stibal, M., Lis, G.P., Butler, C.E.H., Laybourn-Parry, J., Nienow, P., Chandler, D., Dewsbury, P. (2014) Greenland Ice Sheet exports labile organic carbon to the Arctic oceans. *Biogeosciences* 11, 4015-4028.

Qiu, X., Thompson, J.W., Billinge, S.J.L. (2004) PDFgetX2: a GUI-driven program to obtain the pair distribution function from X-ray powder diffraction data. *Journal of Applied Crystallography* 37, 678-678.

Reynolds, B.C., Aggarwal, J., Andre, L., Baxter, D., Beucher, C., Brzezinski, M.A., Engstrom, E., Georg, R.B., Land, M., Leng, M.J., Opfergelt, S., Rodushkin, I., Sloane, H.J., van den Boorn, S.H.J.M., Vroon, P.Z., Cardinal, D. (2007) An inter-laboratory comparison of Si isotope reference materials. *Journal of Analytical Atomic Spectrometry* 22, 561-568.

Savage, P.S., Georg, R.B., Williams, H.M., Burton, K.W., Halliday, A.N. (2011) Silicon isotope fractionation during magmatic differentiation. *Geochimica et Cosmochimica Acta* 75, 6124-6139.